ACS APPLIED ENERGY MATERIALS

www.acsaem.org Article

Composition-Dependent Oxygen Reduction Reaction Activity of Pt-Surfaced PtNi Dodecahedral Nanoframes

Yongchen Wang, Shutang Chen, Xudong Wang, Adam Rosen, William Beatrez, Lukasz Sztaberek, Haiyan Tan, Liang Zhang,* Christopher Koenigsmann,* and Jing Zhao*

Cite This: *ACS Appl. Energy Mater.* 2020, 3, 768−776 Read Online

ACCESS | Metrics & More | Article Recommendations | Supporting Information

ABSTRACT: Pt-based bimetallic nanoframes have been demonstrated to have high activity for a number of electrocatalytic reactions. Their morphology, crystal facets, and compositions are important factors that regulate their catalytic activities. Herein, we synthesized a series of Pt-surfaced PtNi dodecahedral nanoframes with variable Pt/Ni ratios. The nanoframes were prepared by oxidative etching of presynthesized PtNi rhombic dodecahedron nanoparticles. The Pt ratio in the PtNi nanoframes have been tuned from 28% to 65% by changing the duration of oxidative etching. In terms of catalytic performance, the PtNi nanoframes display a volcano-type behavior in specific oxygen reduction reaction (ORR) activity as a function of Pt ratio with a maximum ORR specific activity of 1.9 mA cm^{-2} observed with 47% Pt. The mass activity of the particles ranges from 0.72 to 0.92 A mg^{-1}, which significantly exceeds the mass activity of 0.19 A mg^{-1} measured for commercial Pt NP/C. Density functional theory calculations reveal that the Pt ratio underneath the Pt skin in the nanoframes affects the binding energy of oxygenate species and thus the ORR activity. The trend of OH binding energy versus PtNi composition from the computational results qualitatively agrees with the trend of ORR activity from the experiments.

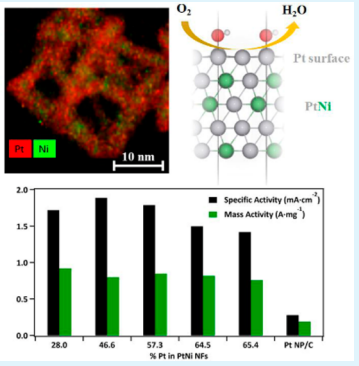

KEYWORDS: *bimetallic nanoparticles, rhombic dodecahedral nanoframes, polymer electrolyte membrane fuel cell, density functional theory, platinum group metal, electrocatalysis*

INTRODUCTION

Polymer electrolyte membrane fuel cells (PEMFC) are a promising renewable energy technology for automotive applications since they can convert chemical energy to electrical energy without producing carbon emissions.[1] A key challenge in the development of these devices is the poor performance and high cost of catalysts for the oxygen reduction reaction (ORR). Among all the monometallic catalysts of ORR, Pt has the best catalytic performance.[2,3] However, the kinetics of ORR are hindered on Pt by the relatively strong binding of oxygen species near the thermodynamic potential for ORR, which results in a significant overpotential.[4−6] To overcome these issues, catalyst performance has been increased by incorporating other less expensive transition metals such as Ni,[5,7−10] Co,[11−15] Cu,[16,17] and Fe[16,18] into Pt. Combining Pt with first-row transition metals leads to a downshift in the Pt d-band center as a result of both structural and electronic effects. A downshift in the Pt d-band center weakens the interaction with oxygen adsorbate[19] and increases ORR kinetics.[20] Recently, further increases in catalytic performance have been achieved by doping in a third metal such as Mo,[21] Ga,[1] Ru,[22] and Rh[23] to form Pt-based ternary alloys.[24]

Among the plethora of first-row transition metals, PtNi-based bimetallic catalysts have shown promising catalytic activity and durability. Specifically, PtNi (111) surface has been reported to have 10-fold higher ORR activity than the corresponding Pt (111) surface and 90-fold higher activity than the commercial Pt/C catalysts.[25] Furthermore, the composition of the PtNi alloy also influences their catalytic activity. In homogeneous alloys, PtNi nanoparticles with 1:1 Pt:Ni ratio exhibited an ∼3-fold enhancement over $PtNi_3$ nanoparticles with a 1:3 Pt:Ni ratio in ORR activity.[26] Cui et al. also observed that in PtNi nanoparticles, when the Ni percentage is varied between 15% and 70%, $Pt_{30}Ni_{70}$ exhibited the highest specific activity for ORR.[27] Composition can also be controlled spatially by dealloying PtNi alloys to form so-called "Pt-skin" nanoparticles, which consist of a platinum-enriched surface and a PtNi alloy core.[28] Tian et al. synthesized one-dimensional bunched platinum−nickel (Pt−Ni) alloy nanocages with a Pt-skin structure, which exhibit higher mass activity and specific activity in ORR compared with the solid 1-D PtNi bunched nanospheres.[28] The interaction between the Pt shell and the PtNi core induces a surface strain[29−31] and a ligand effect[32,33] on the Pt surface sites, thereby improving the catalytic activity of the resulting particle.[34] To further improve

Received: September 30, 2019
Accepted: January 2, 2020
Published: January 2, 2020

https://dx.doi.org/10.1021/acsaem.9b01930
ACS Appl. Energy Mater. 2020, 3, 768−776

the ORR catalytic performance of the PtNi nanoparticles, tailoring their architecture becomes inevitable.[35] Throughout the recent years, a variety of PtNi nanostructures have been reported, such as branched particles,[36,37] double dumbell,[38] core−shell,[5] hyperbranched nanostructures,[39] octahedron,[9,10,40] dodecahedron,[8] icosahedron,[41] hexapods,[42] nanocages,[28] octahedral nanoframes,[43] dodecahedral nanoframes,[7,8,37,44] and multiframes.[45]

Among these nanostructures, hollow, three-dimensional nanoframes represent a promising structural paradigm for the development of ORR catalysts. The hollow nature of nanoframes greatly increases platinum utilization by removing inactive platinum content at the core of the structure and increasing the electrochemically accessible surface area. Moreover, the platinum content in nanoframes is localized at the edges and vertexes of the particle and thus offers high surface area, low-coordinated atoms, steps, and kinks,[46,47] which provide unique active sites for catalysis. Previously, Chen et al. developed a thermal evolution method to synthesize Pt_3Ni polyhedral nanoparticles and dodecahedral nanoframes, and their ORR activities show the following order: Pt/C < PtNi polyhedra/C ≪ Pt_3Ni nanoframes.[8] Chen et al. also demonstrated that PtNi nanoframes exhibited an enhanced ethanol electro-oxidation activity and stability than the Pt−Ni seed-core-frame nanostructures.[44]

To understand the effect of composition and crystal facets on the ORR activity of PtNi nanoframes, we synthesized a series of PtNi rhombic dodecahedral nanoframes via a two-step solution-based process, wherein solid PtNi rhombic dodecahedra undergo oxidative etching to form dodecahedral PtNi nanoframes (see Figure 1). The nanoframes fabricated via

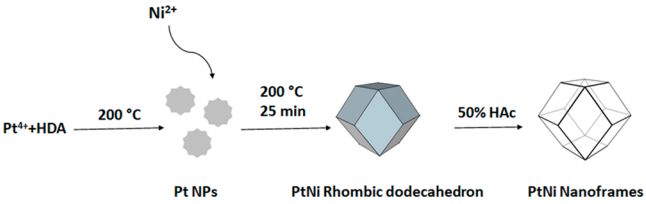

Figure 1. Illustration of the synthetic routes of PtNi rhombic dodecahedral nanoframes.

oxidative etching possess a Pt skin, and the surfaces consist of Pt (111) and some high index facets, as revealed by high-resolution transmission electron microscopy (HRTEM). The composition of the nanoframes can be tuned by varying the etching time. Pt% increased from 28.0% with 2 h of etching to 65.4% with 24 h of etching and plateaued. The nanoframes exhibit composition-dependent catalytic performance for ORR. The Pt-surfaced PtNi nanoframes with a Pt% of 46.6% has the highest catalytic activity of 1.9 mA cm^{-2}. The mass activity of the particles ranges from 0.72 to 0.92 A mg^{-1}. The impact of composition on catalytic performance was studied by density functional theory (DFT) simulations,[48−50] and we found that the leaching of Ni initially improves the weak binding of surface oxygenated species and reaches the top of activity volcano at a Pt% of 60% theoretically.

EXPERIMENTAL METHODS

Chemicals. Chloroplatinic acid hexahydrate ($H_2PtCl_6·6H_2O$, ACS reagent, ≥37.50% Pt basis), hexadecylamine (HDA, 98%), oleylamine (OLA, 70%), and polyvinylpyrrolidone (PVP, powder, average M_w ~ 55000) were purchased from Sigma-Aldrich. Nickel acetylacetonate ($Ni(acac)_2$, 96%) was purchased from Acros Organics. Perchloric acid (Optima grade) was purchased from Fisher Scientific. Commercial carbon supported platinum nanoparticles (Pt NP/C, HiSpec, 20% Pt loading) were purchased from Alfa Aesar. All chemicals were used as received without any purification.

Synthesis of PtNi Rhombic Dodecahedron. The PtNi polyhedral nanoparticles capped with HDA were synthesized through the following procedure. HDA (40 mmol, 10.0 g) and $H_2PtCl_6·6H_2O$ (0.1 mmol, 51.7 mg) were added into a 50 mL three-neck flask equipped with a magnetic stir bar. The reaction system was degassed by nitrogen gas throughout the whole experiment to remove O_2. The temperature was increased to 200 °C, and the reaction mixture quickly turned gray under stirring. As soon as the reaction mixture changed color, $Ni(acac)_2$ (0.2 mmol, 51.2 mg) in 2 mL of OLA was injected into the reaction mixture. The reaction temperature was kept at 200 °C for another 25 min. After the reaction, ethanol was added and the mixture was centrifuged at 5000 rpm for 5 min to remove excess reactants and surfactants.

Synthesis of PtNi Rhombic Dodecahedral Nanoframes. PtNi polyhedral NPs (30 mg), 4.0 mL of PVP ethanol solution (2 mg/mL), and 20.0 mL of 50% (volume ratio) acetic acid in ethanol were added to a scintillation vial equipped with a magnetic stir bar. The mixed solution was sonicated for 5 min, and it turned black. The solution was then stirred for different durations (2, 6, 8, 16, and 24 h) at 60 °C by using a hot water bath. The products were precipitated out by adding ethanol to the solution and separated by centrifugation at 5000 rpm for 2 min. The final product was redispersed in ethanol.

Characterization. Transmission electron microscopy (TEM) images, high angle annular dark field scanning transmission electron microscopy (HAADF-STEM) images, and energy-dispersive X-ray (EDX) mapping images were all obtained using a FEI-Talos microscope at an accelerating voltage of 200 kV and a FEI-Themis microscope at an accelerating voltage of 300 kV. XRD was acquired on a Bruker D2 phaser diffractometer using a Cu Kα source. Inductively coupled plasma mass spectrometry (ICP-MS, Thermo-Electron X Series) was used to determine the platinum loading in the final catalyst inks. X-ray photoelectron spectroscopy was performed with a PHI 5000 VersaProbe II instrument equipped with an Al Kα X-ray source. XPS samples were prepared by supporting the PtNi NF powders onto ultraflat Si wafers. The data were collected with a 50 W beam and a 200 μm spot size at an accelerating voltage of 15 kV. Survey scans were performed with a 187.5 eV analyzer pass energy at 0.8 eV per step averaged from a total of 10 scans. High-resolution scans were performed with an analyzer pass energy of 23.5 at 0.1 eV per step and were averaged from a total of 20 scans. High-resolution scans of the Pt 4f and 4d peaks were referenced to the C 1s peak.

Electrochemical Analysis. Electrochemical measurements were performed on a Pine Instrument WaveDriver20 bipotentiostat equipped with an MSR rotator for rotating disk electrode (RDE) measurements. A custom electrochemical cell was assembled with a platinum counter electrode (3.0 cm^2 active area) and a Ag/AgCl reference electrode (3 M Cl^-) housed in a double junction chamber (BASi Instruments). All potentials are reported with respect to the reversible hydrogen electrode (RHE). A glassy carbon rotating disk electrode (GC-RDEs, Pine Instruments, 5 mm) served as the working electrode and was polished to a mirror finish with an alumina slurry prior to use. The surface of the electrode was premodified with a thin carbon layer to improve the dispersion of the unsupported PtNi nanoframes. A Vulcan carbon ink (1 mg mL^{-1}) was prepared in 25% isopropanol, and 10 μL was drop-cast onto the surface and allowed to dry in air. Catalyst inks were prepared by dispersing the PtNi nanoframe powders or commercial Pt NP/C into ethanol solution with a concentration of 2 mg mL^{-1}. The catalyst was loaded onto the electrode by drop-casting 5 μL of the catalyst ink onto the premodified electrode surface and allowing the drop to dry in air. Because of variations in the yield of the reaction, the concentration of the PtNi nanoframe inks and the loading varied from sample to sample. ICPMS measurements were performed on the catalyst inks to determine the precise Pt content on the electrode. The electrode was sealed by drop-casting 5 μL of a 0.025% Nafion solution prepared in

https://dx.doi.org/10.1021/acsaem.9b01930
ACS Appl. Energy Mater. 2020, 3, 768−776

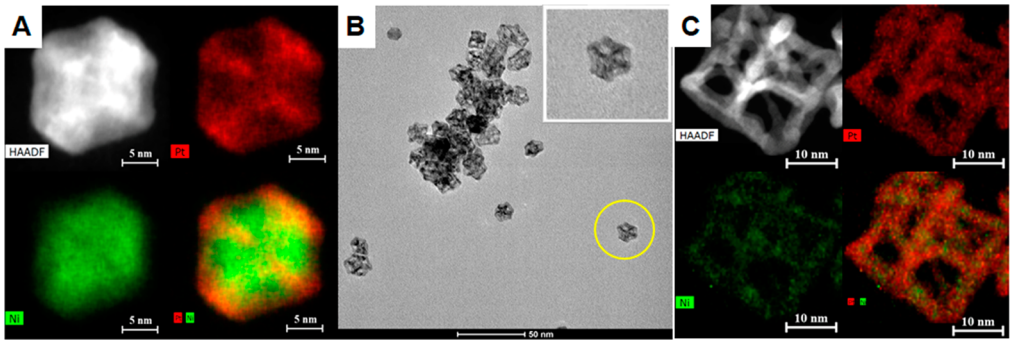

Figure 2. (A) HAADF-STEM image and EDS mapping of a typical rhombic dodecahedron. Pt is marked in red while Ni in green. (B) TEM images of rhombic dodecahedral nanoframes. (C) HAADF-STEM image and EDS mapping of representative rhombic dodecahedral nanoframes that consist of Pt (red) and Ni (green).

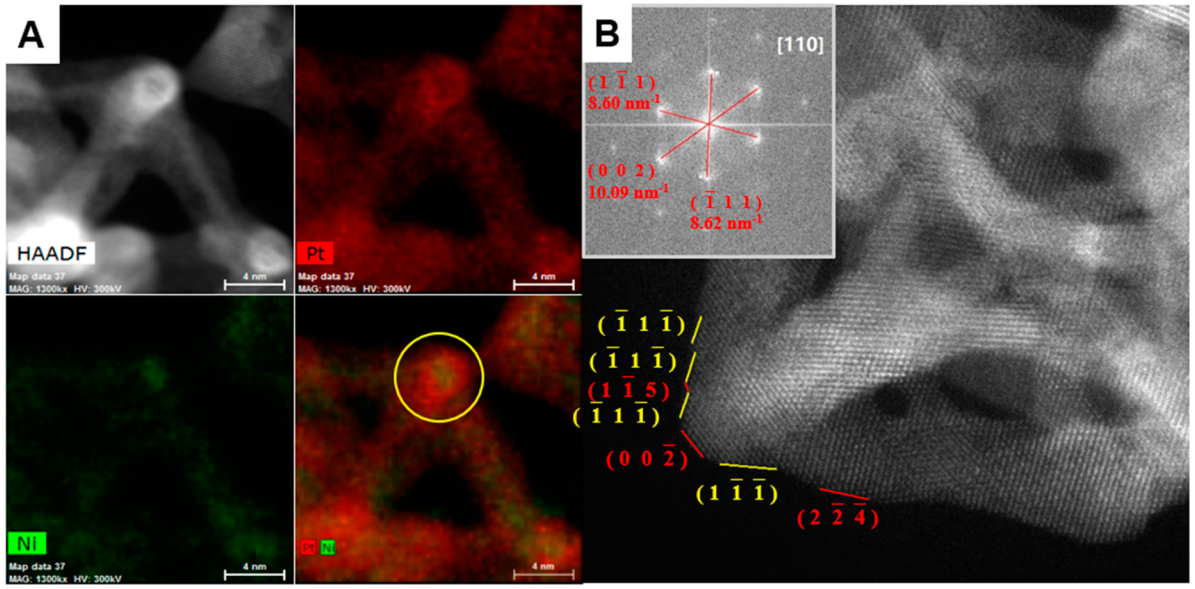

Figure 3. (A) HAADF-STEM image and EDS mapping of a part of a representative rhombic dodecahedral nanoframe. Pt is marked in red while Ni in green. (B) High-resolution STEM (HRSTEM) image of a PtNi nanoframe with edges indexed with corresponding facets with its fast Fourier transformation image.

ethanol on the surface. Prior to electrochemical measurements the GC-RDE was immersed into ultrapure water (18.2 MΩ·cm, Millipore DirectQ5) to remove impurities and hydrate the film.

Cyclic voltammograms were obtained with a scan rate of 20 mV s^{-1} in deoxygenated 0.1 M perchloric acid prepared by diluting the concentrated acid in ultrapure water. Polarization curves were obtained in oxygen-saturated 0.1 M $HClO_4$ at a rotation rate of 1600 rpm and a scan rate of 20 mV s^{-1}. The electrochemically accessible surface area of Pt was determined from the integrated hydrogen adsorption charge (H_{ads}) in the cyclic voltammogram utilizing the conversion factor 0.21 mC cm^{-2}. The capacitive contribution of the electrode and Vulcan carbon layer was removed during the integration of the H_{ads} peaks. The durability of the catalysts was examined by using a method outlined by the US Department of Energy adapted for testing ORR catalysts under half-cell conditions.[51] The potential is cycled between 0.6 and 1.0 V at a rate of 50 mV s^{-1} in a 0.1 M $HClO_4$ solution exposed to the atmosphere. The electrochemical surface area (ECSA) and activity are determined before and after 5000 cycles.

Simulation Methods. All binding energies were calculated by using density functional theory (DFT) implemented in the Quantum ESPRESSO Package. Kohn−Sham wave functions were expanded in a plane-wave basis with a kinetic energy cutoff of 500 eV. The exchange-correlation energy was evaluated by generalized gradient approximations (GGA) using the Perdew−Burke−Ernzerhof (PBE) method. All geometries were considered optimized when the force on each atom was <0.03 eV/Å. Atomic structure optimization was done with a 4 × 4 × 1 *k*-point grid for (111) surfaces and a (4 × 3 × 1) grid for (211) surfaces. Both plane wave cutoffs and *k*-point grid density were checked for convergence with respect to chemisorption energies. A vacuum gap of at least 14 Å in the *z* direction is used to avoid interactions from periodic images.

The (111) and (211) surfaces were modeled with a five-layer (2 × 2) slab and (2 × 1), respectively. The topmost layer was kept as Pt skin, and the top three layers were set free to move during structural optimization. For each subsurface alloy composition, ten different random-alloy configurations were generated to calculate the average OH binding energy.

■ RESULTS AND DISCUSSION

Pt-surfaced PtNi rhombic dodecahedral nanoframes were synthesized by following an oxidative etching method[44] with minor modification, as illustrated in Figure 1. In this method, $H_2PtCl_6·6H_2O$ and $Ni(acac)_2$ were the metal precursors, and hexadecylamine (HDA) served as the reducing agent, surface ligand, and solvent. $H_2PtCl_6·6H_2O$ was mixed with HDA and heated to 200 °C. Pt(IV) was quickly reduced to irregular-shaped Pt seeds by HDA. Ni precursors were then added to

https://dx.doi.org/10.1021/acsaem.9b01930
ACS Appl. Energy Mater. 2020, 3, 768−776

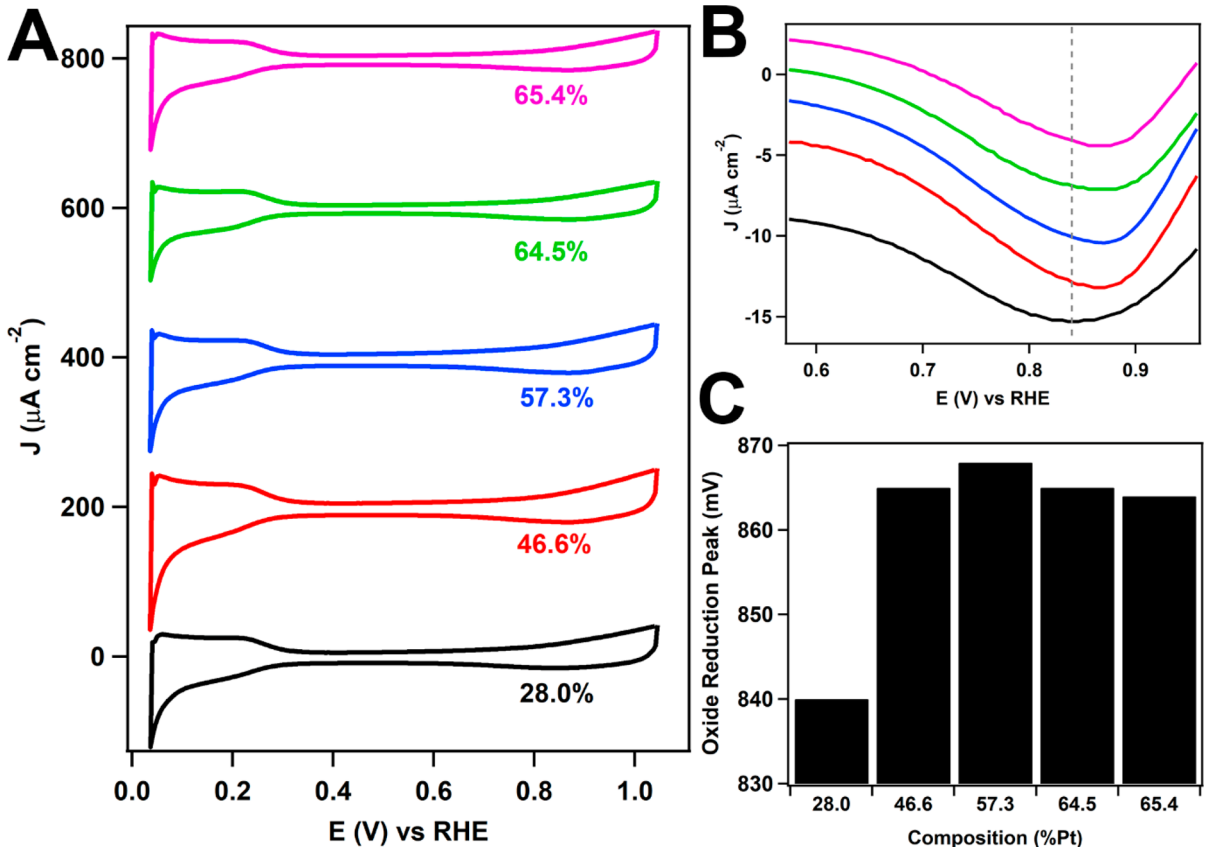

Figure 4. Cyclic voltammograms (A) of PtNi nanoframes as a function of Pt content. The cathodic oxide reduction peaks (B) and the trend in oxide reduction peak potential with respect to composition (C) are also shown.

the reaction solution containing Pt seeds. After heating at 200 °C for 25 min, rhombic dodecahedral PtNi nanoparticles were obtained (see Figures S1 and 2A). Figure 2A shows a typical high-angle annular dark-field scanning transmission electron microscopy (HAADF/STEM) image of the PtNi nanostructures, of which the corner-to-corner distance was determined to be 35.6 ± 5.7 nm based on Figure S1A. Energy dispersive X-ray spectroscopy (EDS) elemental images show that Pt mainly appears on the edges and corners of the polyhedron, while Ni remains in bulk. By oxidative etching using acetic acid (HAc), the PtNi polyhedron nanoparticles turned into PtNi dodecahedral nanoframes. The size of the nanoparticles remains approximately the same (30.6 ± 3.2 nm) as the etching process goes on. Figure 2B shows typical TEM images and zoomed-in images of the PtNi dodecahedral nanoframes. The length of the edges is determined to be 13.6 ± 1.6 nm, and the width of the edges is determined to be 2.9 ± 0.5 nm. Figure 2C reveals that after the acid etching process bulk Ni is completely removed. In the nanoframes, Ni remains in the middle of the skeleton; in contrast, Pt distributes both in the skeleton and on the skin of the nanoframes. The corresponding EDS line profile in Figure S2 further confirmed that a few layers of Pt were on the coating on the PtNi skeleton. In a zoomed-in high-resolution scanning transmission electron microscope (HRSTEM) image and the EDS maps of the nanoframes (Figure 3A), we also found a core−shell-like structure within the vertex of a nanoframe, where a Pt shell appeared on a Ni core. This phenomenon is further confirmed by corresponding EDS line profile (Figure S2). HRSTEM was also used to index the facets on the edges of a nanoframe, in which Pt (111) facets and some high Miller index facets were observed (Figure 3B). The corresponding fast Fourier transformation image (Figure 3B) shows the single crystalline nature of the nanoframe.

The composition of bimetallic nanoparticles has a significant impact on their catalytic activities. In our synthesis of the nanoframes, the composition of the nanoframes can be easily tuned by varying the oxidative etching time. Thus, we monitored the composition and morphology change of the nanoparticles at variable etching durations using TEM, EDS mapping, XRD, and ICP-MS. During etching, the content of Ni decreased quickly at the beginning because of the leaching out of bulk nickel and gradually plateaued (Figure S3). As Figure S4 shows, the surface of the dodecahedral nanoparticles is thin, and the structures are partially hollow at 2 h of etching. The X-ray diffraction pattern (Figure S7) shows that there is still a significant Ni (111) peak, which means bulk Ni has not been completely removed yet. However, after 6 h of etching, the Ni (111) peak can no longer be found, and the main PtNi (111) peak shifts towards a lower angle, indicating a higher percentage of Pt in the sample. TEM and HAADF-STEM images as well as EDS mapping images of the samples acquired at 6 h (Figure S5) also suggest that bulk Ni has completely been removed, and the nanostructure becomes hollow. After the first 6 h, the rate of Ni dissolution decreases, leading to a plateau in the composition of the particle after 24 h of etching. We attribute it to the existence of the "Pt skin" outside Ni, which protects Ni in the vertex and skeleton from being further oxidized and etched away. Despite the significant change in

https://dx.doi.org/10.1021/acsaem.9b01930
ACS Appl. Energy Mater. 2020, 3, 768−776

Table 1. Composition and Electrochemical Data of the PtNi Nanoframes Acquired at Different Etching Times

etching time (h)	composition (%Pt)	ECSA[a] (m^2 g^{-1})	oxide reduction peak (mV vs RHE)	specific activity (mA cm^{-2})	Pt mass activity (A mg^{-1})
2	28.0	53.1	840	1.72	0.92
6	46.6	42.0	865	1.89	0.80
8	57.3	47.2	868	1.79	0.85
16	64.5	54.7	865	1.50	0.82
24	65.4	53.5	864	1.42	0.76
Pt NP/C	100	90.0[b]	798	0.28	0.19

[a]The electrochemically accessible surface area of Pt was determined from the integrated hydrogen adsorption charge in the CV. Platinum loading was determined from ICPMS data collected from the catalyst ink. [b]Value reported from a HiSpec 3000 Pt nanoparticle specification sheet.

composition, the morphology of the nanoframes remains the same after 6 h of etching time (Figure S6).

The surface composition of the PtNi NFs was investigated by XPS spectroscopy prior to electrochemical characterization, and the data are shown in Figures S8 and S9. Survey scans reveal that there are small but detectable Ni peaks in the 28.0% and 46.6% samples, suggesting that Ni is present at the surface of the particles. However, the intensity of the Ni peaks decreases significantly in the spectra with higher Pt content and are not detectable above 60% Pt. This suggests that Pt is enriched at the surface of the particles, which is consistent with the EDS line scan data in Figure S2. High-resolution scans of the Pt 4f and 4d regions were collected, and the peak positions are summarized in Table S1. High-resolution scans revealed that the Pt $4f_{7/2}$, $4f_{5/2}$, $4d_{5/2}$, and $4d_{3/2}$ peaks of the PtNi NFs were located at 70.4, 73.7, 314.1, and 331.3 eV, respectively. The Pt 4f peaks were shifted by 1 eV to lower binding energies compared with the commercial Pt NP/C sample, which was observed at 74.7 eV.[52] The shift in the binding energy provides further evidence that the PtNi alloy at the core of the material influences the electronic properties of the Pt surface sites.

Cyclic voltammetry (CV) was employed to evaluate the electrochemical properties of the PtNi nanoframes as a function of etching time. Initially, the surfaces of the catalyst particles were activated by cycling the potential to +1.3 V at a rate of 100 mV s^{-1} to oxidize residual organic impurities. A significant irreversible oxidation wave was observed in each of the catalyst samples above 1.0 V consistent with oxidation of adsorbed acetate species.[53] The nanoframes etched for 2 h also displayed a broad irreversible oxidation wave between 0.3 and 0.5 V in the first cycle. This can be attributed to the oxidation and dissolution of surface Ni and bulk Ni present at the core of these structures.[54] The oxidation of Ni was not observed in the catalysts (Figure S10) with etching times above 2 h. This finding is consistent with the XPS and HRTEM results and suggests that bulk Ni is fully removed and that a platinum skin is formed in the samples after 6 h of etching time. Because Ni oxidation is observed in the sample with a 2 h etching time, the surface is enriched with Pt but does have Ni present prior to electrochemical measurements.

The CVs obtained from the PtNi nanoframes as a function of etching time are shown in Figure 4. The characteristic hydrogen adsorption/desorption (0−0.4 V) and surface oxide regions (0.6−1.0 V) are consistent with the presence of a Pt-rich, nanostructured surface. The structure of the hydrogen adsorption does not change significantly as a function of etching time, which suggests that a platinum skin is formed by the etching process.[55] In addition, this phenomenon suggests that the effects of the capping agents employed in the synthesis are consistent among the various samples. If the surface contained a mixture of Pt and Ni sites, the hydrogen adsorption charge would increase with increasing platinum content. Because Ni is readily leached from the surface, the density of Ni sites is expected to be very low regardless of the overall concentration of Ni in the particle. Table 1 summarizes the composition, ECSA, oxide reduction peak, and specific and mass activities of the nanoframes obtained at varying times. The average ECSA for the PtNi nanoframes was 51 ± 5 m^2 g^{-1}, which was lower than that reported value for the commercial Pt NP/C. The lower ECSA is attributed to the fact that the PtNi nanoframes were unsupported, which may contribute to aggregation on the electrode surface. In spite of the low ECSA, the mass activity of the catalysts was considerably larger than that of the Pt NP/C highlighting the benefits of the nanoframe architecture.

The change in composition at different etching times has a measurable effect on the oxide region, which is enlarged in Figure 4B. The positions of oxide reduction peaks in the cathodic sweep were determined from fits of the reduction wave and plotted as a function of platinum concentration (Figure 4C). The oxide reduction peak potential shows a volcano-type dependence as a function of Pt content with the maximum reduction potential of 868 mV observed in 57.3% Pt sample. The observed peak potentials for the PtNi nanoframes were shifted by +40 mV to +70 mV relative to peak observed in the CV (Figure S11) for commercial Pt NP/C. Positive shifts in the oxide reduction peak are correlated with weaker interactions with oxygen adsorbates and are expected to lead to increased ORR performance.[20]

Polarization curves were obtained in oxygen-saturated solution to evaluate the ORR performance of the catalysts. The specific activity (J_K) was determined at 0.9 V by normalizing the kinetic current (I_K) for ORR to the electrochemically accessible surface area determined from the integrated hydrogen adsorption charge.[56] Analogous to the trend in the position of the oxide reduction peak, the catalytic activity of the PtNi nanoframes displays a volcano-type dependence as a function of etching time (Figure 5B) with a peak performance of 1.9 mA cm^{-2} for the 6 h etching time (46.6% Pt). The PtNi nanoframes displayed significantly enhanced specific activity of over 6-fold relative to the activity of 0.28 mA cm^{-2} for Pt NP/C. The 28.0% sample displays the highest mass activity of 0.92 A mg^{-1}, which is consistent with the low platinum content of this sample and is more than 4-fold higher than the activity of 0.19 A mg^{-1} determined for the Pt NP/C. Although the 46.4% has the highest specific activity, the increase in platinum content outweighs the increase in specific activity leading to a slightly lower mass activity. In the remaining samples, the relative change in the platinum content was lower, and we observed slightly less aggregation of the particles with increased platinum content. These factors account for a stable mass activity despite the decrease in the

https://dx.doi.org/10.1021/acsaem.9b01930
ACS Appl. Energy Mater. 2020, 3, 768−776

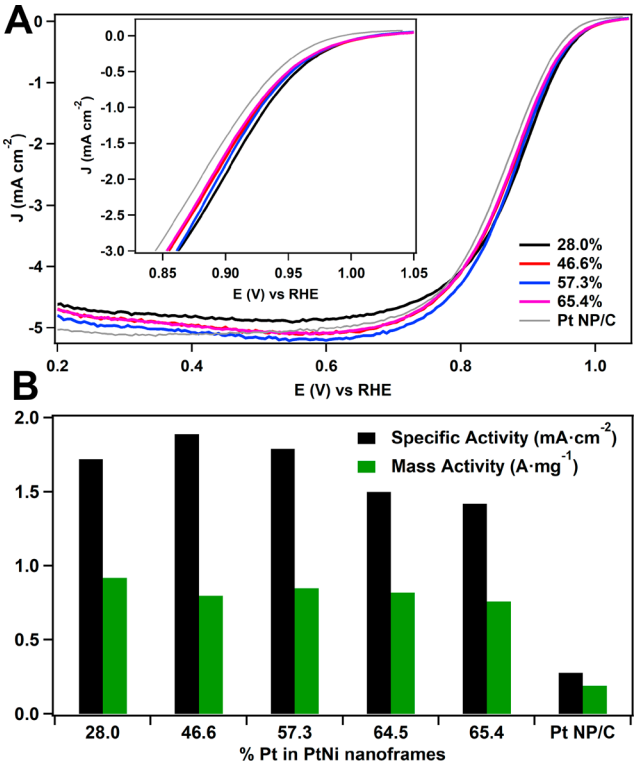

Figure 5. ORR polarization curves of PtNi nanoframes (A) collected in oxygen-saturated 0.1 M $HClO_4$ at a rotation rate of 1600 rpm. The onset region of the polarization curve is highlighted as an inset. The specific and Pt mass activities as a function of nanoframe composition (B) are shown in comparison with Pt NP/C.

specific activity. Over the entire composition regime, the mass activity of the PtNi nanoframes samples are approximately 2-fold higher than the U.S. Department of Energy mass activity target of 0.44 A mg^{-1} projected for 2020.[51]

To examine the long-term durability of the catalysts, we obtained polarization curves before and after a 5000-cycle extended durability test (Figure S11) for ORR catalysts. The extended durability test resulted in a relatively small 10 mV shift in the half-wave potential of the polarization curve. This was associated with a 14% decrease in the ECSA measured from CVs before and after the extended durability test. A slight increase of 7 mV in the oxide reduction peak potential was observed and is consistent with the oxidative etching effect of low-coordination atoms and defect sites. By contrast, commercial Pt NP/C tested under identical conditions had much lower overall durability with a 16 mV shift in the half-wave potential and a decrease in the ECSA of 38.7%. This indicates that the PtNi NFs have better durability relative to a pure Pt analogue.

Furthermore, OH binding energies on the Pt skin were calculated by using DFT to computationally assess the ORR activity and to understand the experimental specific activity trend. Nørskov et al. showed that the surface reactivity, such as O or OH binding energy, is an effective descriptor of the ORR activity.[20] It has also been shown that the rate-limiting step in ORR on transition metal surfaces is the dissociation of O_2 or the removal of oxygenated species on the surface. ORR on noble metals (weak binding), e.g., Au and Ag, is hindered by the sluggish kinetics of O_2 dissociation. On the other hand, protonation of surface oxygenated species limits the ORR activity on reactive metals (strong binding). Therefore, a volcano-shaped ORR activity trend was found as a function of the binding energy of surface oxygenated species. Among all the single crystal transition metals, Pt is the closest one to the top of the ORR activity volcano and provides the best trade-off between the above two factors, which is only ~0.2 eV stronger than the top of the volcano in terms of OH binding energy.[20]

The blue scatters in Figures 6 show OH binding energies on Pt (111) surface with different subsurface Ni−Pt alloy composition (Pt% = 25%, 50%, 75%, and 100%) with respect to the OH binding energy on Pt (111). As indicated by the solid line, the OH binding on the Pt (111) skin is nearly linearly weakened by the increase of subsurface Ni ratio. Interestingly, such a linear dependence was also found in other alloy-core@shell systems, e.g., AuPd@Pt.[57,58] The experimentally measured ORR activity trend can also be qualitatively explained by the calculated OH binding energy trend. When the etching time is short (2 h), the subsurface of the nanoframes is dominated by Ni content (Pt% = 28.0%), resulting in a weak surface OH binding. Elongated etching time reduces the subsurface Ni concentration, which in turn shift the ORR activity from the right branch toward the top of the volcano. The optimal ORR activity (ΔEb_{OH} = ~0.2 eV) is then achieved when the subsurface Pt% is increased to the 60%. Further etching process continues the loss of Ni content in the subsurface and leads to an OH overbinding surface, which in turn causes the drop of activity.

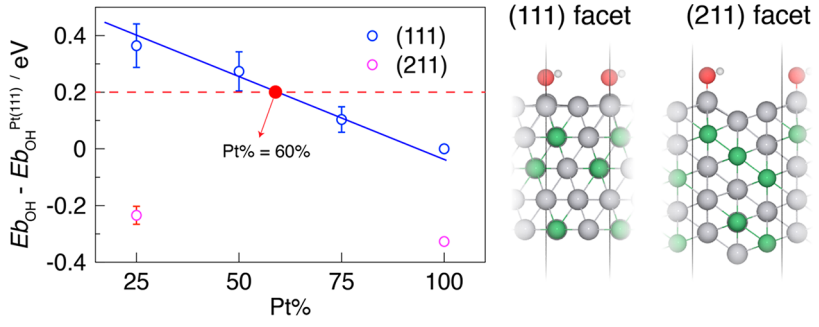

Figure 6. DFT calculated OH binding energies on Pt (111) and (211) surfaces with different subsurface Pt alloy ratios, as shown in blue and pink scatters. All energies are plotted with respect to the OH binding energy on the Pt (111) surface. The intersection of the (111) surface trendline and the red dashed line (top of the activity volcano) gives an estimation of the optimal subsurface composition at Pt% = 60%. Error bars on the plot show the distribution of surface OH binding energies of the given subsurface alloy composition. Example atomic structures of (111) and (211) Pt surfaces with Pt−Ni subsurface alloy are also illustrated on the right two panels. Gray: Pt; green: Ni; red: O; and white: H.

https://dx.doi.org/10.1021/acsaem.9b01930
ACS Appl. Energy Mater. 2020, 3, 768−776

As illustrated by the pink scatters in Figure 6, (211) surfaces are also computed to understand the activity change of high-index facets. It is clear that the Pt (211) surface binds OH too strongly as compared to the Pt (111) surface with suppressed ORR activity. The effect of subsurface alloying on the surface reactivity is also found to be less significant on high-index facets than the (111) surface. Thus, the active sites of the nanoframes are most likely from the (111) facets.

Although the OH binding energy is an excellent descriptor of ORR activity, the trend in specific activity peaks at a slightly lower composition of ~47%. The mechanism of ORR on nanostructured platinum is complex and involves a series of mechanistic steps involving the adsorption of molecular oxygen, bond dissociation, protonation, and water desorption.[59] In this case, the oxygen binding energy provides a useful tool for estimating trends in experimental ORR performance. However, the complexity of the structure in terms of both the uniformity of composition and the surface structure and the experimental uncertainties in the composition determination could lead to the small discrepancy in the composition-dependent ORR trend.

CONCLUSIONS

In this work, we developed a synthetic protocol to produce PtNi dodecahedral nanoframes via oxidative etching of solid PtNi rhombic dodecahedron nanoparticles by acetic acid. The PtNi nanoframes have a Pt skin and a PtNi skeleton underneath. The Pt percentage in the PtNi skeleton (controlled by the etching time) has an impact on the ORR activity of the nanoframes. The ORR activity of the nanoframes increases and then decreases with increasing acetic acid etching time and reaches the top of activity volcano at 6 h of etching, with a specific activity of 1.9 mA cm^{-2}. Although the surface of the nanoframes is composed of Pt, the Pt percentage underneath the Pt surface layer still affects the binding energy of oxygenate species, as revealed by DFT calculations. This study reveals the significance of the composition of sublayer and also provides guidance for further tuning and improving the performance of Pt-based alloy nanocatalysts.

ASSOCIATED CONTENT

Supporting Information

The Supporting Information is available free of charge at https://pubs.acs.org/doi/10.1021/acsaem.9b01930.

Additional TEM, HAADF-STEM images and EDS mapping images, XRD patterns, showing the compositions of the nanoframes, and electrochemical data (PDF)

AUTHOR INFORMATION

Corresponding Authors

Liang Zhang − *University of Connecticut, Storrs, Connecticut;* orcid.org/0000-0002-9718-0436; Email: liang.zhang-cbe@uconn.edu

Christopher Koenigsmann − *Fordham University, Bronx, New York;* orcid.org/0000-0002-2870-1509; Email: ckoenigsmann@fordham.edu

Jing Zhao − *University of Connecticut, Storrs, Connecticut;* orcid.org/0000-0002-6882-2196; Email: jing.zhao@uconn.edu

Other Authors

Yongchen Wang − *University of Connecticut, Storrs, Connecticut;* orcid.org/0000-0003-0792-2908

Shutang Chen − *University of Connecticut, Storrs, Connecticut*

Xudong Wang − *University of Connecticut, Storrs, Connecticut;* orcid.org/0000-0002-1189-8181

Adam Rosen − *Fordham University, Bronx, New York*

William Beatrez − *Fordham University, Bronx, New York*

Lukasz Sztaberek − *Fordham University, Bronx, New York, and New York City College of Technology, Brooklyn, New York*

Haiyan Tan − *University of Connecticut, Storrs, Connecticut*

Complete contact information is available at: https://pubs.acs.org/10.1021/acsaem.9b01930

Notes

The authors declare no competing financial interest.

ACKNOWLEDGMENTS

This work was supported in part by the Thermo Fisher Scientific Graduate Fellowship awarded to Y.W. The TEM studies were performed using the facilities in the UConn/Thermo Fisher Scientific Center for Advanced Microscopy and Materials Analysis (CAMMA). A.R., W.B., and C.K. thank Fordham College at Rose Hill for research support through Undergraduate Research Grants. C.K. also thanks Professor Jon Friedrich for his assistance with collecting ICPMS data and the Yale West Campus Materials Characterization Core for access to their XPS instrument. L.Z. is thankful for the use of the computer time allocation at the Extreme Science and Engineering Discovery Environment (XSEDE) supported through National Science Foundation under Award CHE160084.

REFERENCES

(1) Lim, J.; Shin, H.; Kim, M.; Lee, H.; Lee, K.-S.; Kwon, Y.; Song, D.; Oh, S.; Kim, H.; Cho, E. Ga-Doped Pt-Ni Octahedral Nanoparticles as a Highly Active and Durable Electrocatalyst for Oxygen Reduction Reaction. *Nano Lett.* **2018**, *18*, 2450−2458.

(2) Gasteiger, H. A.; Markovic, N. M. Just a Dream—or Future Reality? *Science* **2009**, *324* (5923), 48−49.

(3) Liu, H.; Zhong, P.; Liu, K.; Han, L.; Zheng, H.; Yin, Y.; Gao, C. Synthesis of ultrathin platinum nanoplates for enhanced oxygen reduction activity. *Chemical Science* **2018**, *9*, 398−404.

(4) Debe, M. K. Electrocatalyst approaches and challenges for automotive fuel cells. *Nature* **2012**, *486*, 43−51.

(5) Gan, L.; Heggen, M.; Rudi, S.; Strasser, P. Core-Shell Compositional Fine Structures of Dealloyed PtxNi1-x Nanoparticles and Their Impact on Oxygen Reduction Catalysis. *Nano Lett.* **2012**, *12*, 5423−5430.

(6) Lee, S. W.; Chen, S.; Suntivich, J.; Sasaki, K.; Adzic, R. R.; Shao-Horn, Y. Role of Surface Steps of Pt Nanoparticles on the Electrochemical Activity for Oxygen Reduction. *J. Phys. Chem. Lett.* **2010**, *1* (9), 1316−1320.

(7) Becknell, N.; Son, Y.; Kim, D.; Li, D.; Yu, Y.; Niu, Z.; Lei, T.; Sneed, B. T.; More, K. L.; Markovic, N. M.; Stamenkovic, V. R.; Yang, P. Control of Architecture in Rhombic Dodecahedral Pt-Ni Nanoframe Electrocatalysts. *J. Am. Chem. Soc.* **2017**, *139*, 11678−11681.

(8) Chen, C.; Kang, Y.; Huo, Z.; Zhu, Z.; Huang, W.; Xin, H. L.; Snyder, J. D.; Li, D.; Herron, J. A.; Mavrikakis, M.; Chi, M.; More, K. L.; Li, Y.; Markovic, N. M.; Somorjai, G. A.; Yang, P.; Stamenkovic, V.

R. Highly Crystalline Multimetallic Nanoframes with Three-Dimensional Electrocatalytic Surfaces. *Science* **2014**, *343*, 1339−1343.
(9) Choi, S.-I.; Xie, S.; Shao, M.; Odell, J. H.; Lu, N.; Peng, H.-C.; Protsailo, L.; Guerrero, S.; Park, J.; Xia, X.; Wang, J.; Kim, M. J.; Xia, Y. Synthesis and Characterization of 9 nm Pt-Ni Octahedra with a Record High Activity of 3.3 A/mg Pt for the Oxygen Reduction Reaction. *Nano Lett.* **2013**, *13*, 3420−3425.
(10) Ma, Y.; Miao, L.; Guo, W.; Yao, X.; Qin, F.; Wang, Z.; Du, H.; Li, J.; Kang, F.; Gan, L. Modulating Surface Composition and Oxygen Reduction Reaction Activities of Pt-Ni Octahedral Nanoparticles by Microwave-Enhanced Surface Diffusion during Solvothermal Synthesis. *Chem. Mater.* **2018**, *30*, 4355−4360.
(11) Becknell, N.; Zheng, C.; Chen, C.; Yu, Y.; Yang, P. Synthesis of $PtCo_3$ polyhedral nanoparticles and evolution to Pt_3Co nanoframes. *Surf. Sci.* **2016**, *648*, 328−332.
(12) Li, J.; Jilani, S. Z.; Lin, H.; Liu, X.; Wei, K.; Jia, Y.; Zhang, P.; Chi, M.; Tong, Y. J.; Xi, Z.; Sun, S. Ternary CoPtAu Nanoparticles as a General Catalyst for Highly Efficient Electro-oxidation of Liquid Fuels. *Angew. Chem., Int. Ed.* **2019**, *58*, 11527−11533.
(13) Hu, S.; Tian, M.; Ribeiro, E. L.; Duscher, G.; Mukherjee, D. Tandem laser ablation synthesis in solution-galvanic replacement reaction (LASiS-GRR) for the production of PtCo nanoalloys as oxygen reduction electrocatalysts. *J. Power Sources* **2016**, *306*, 413−423.
(14) Hu, S.; Goenaga, G.; Melton, C.; Zawodzinski, T. A.; Mukherjee, D. PtCo/CoOx nanocomposites: Bifunctional electrocatalysts for oxygen reduction and evolution reactions synthesized via tandem laser ablation synthesis in solution-galvanic replacement reactions. *Appl. Catal., B* **2016**, *182*, 286−296.
(15) Hu, S.; Cheng, K.; Ribeiro, E. L.; Park, K.; Khomami, B.; Mukherjee, D. A facile and surfactant-free route for nanomanufacturing of tailored ternary nanoalloys as superior oxygen reduction reaction electrocatalysts. *Catal. Sci. Technol.* **2017**, *7* (10), 2074−2086.
(16) Lu, L.; Chen, S.; Thota, S.; Wang, X.; Wang, Y.; Zou, S.; Fan, J.; Zhao, J. Composition Controllable Synthesis of PtCu Nanodendrites with Efficient Electrocatalytic Activity for Methanol Oxidation Induced by High Index Surface and Electronic Interaction. *J. Phys. Chem. C* **2017**, *121*, 19796−19806.
(17) Zhang, Z.; Luo, Z.; Chen, B.; Wei, C.; Zhao, J.; Chen, J.; Zhang, X.; Lai, Z.; Fan, Z.; Tan, C.; Zhao, M.; Lu, Q.; Li, B.; Zong, Y.; Yan, C.; Wang, G.; Xu, Z. J.; Zhang, H. One-Pot Synthesis of Highly Anisotropic Five-Fold-Twinned PtCu Nanoframes Used as a Bifunctional Electrocatalyst for Oxygen Reduction and Methanol Oxidation. *Adv. Mater.* **2016**, *28*, 8712−8717.
(18) Jung, C.; Lee, C.; Bang, K.; Lim, J.; Lee, H.; Ryu, H. J.; Cho, E.; Lee, H. M. Synthesis of Chemically Ordered Pt3Fe/C Intermetallic Electrocatalysts for Oxygen Reduction Reaction with Enhanced Activity and Durability via a Removable Carbon Coating. *ACS Appl. Mater. Interfaces* **2017**, *9*, 31806−31815.
(19) Wang, Y.-Y.; Chen, D.-J.; Allison, T. C.; Tong, Y. J. Effect of surface-bound sulfide on oxygen reduction reaction on Pt: Breaking the scaling relationship and mechanistic insights. *J. Chem. Phys.* **2019**, *150* (4), 041728.
(20) Norskov, J. K.; Rossmeisl, J.; Logadottir, A.; Lindqvist, L.; Kitchin, J. R.; Bligaard, T.; Jonsson, H. Origin of the overpotential for oxygen reduction at a fuel-cell cathode. *J. Phys. Chem. B* **2004**, *108* (46), 17886−17892.
(21) Jia, Q.; Zhao, Z.; Cao, L.; Li, J.; Ghoshal, S.; Davies, V.; Stavitski, E.; Attenkofer, K.; Liu, Z.; Li, M.; Duan, X.; Mukerjee, S.; Mueller, T.; Huang, Y. Roles of Mo Surface Dopants in Enhancing the ORR Performance of Octahedral PtNi Nanoparticles. *Nano Lett.* **2018**, *18*, 798−804.
(22) Huang, L.; Zhang, X.; Wang, Q.; Han, Y.; Fang, Y.; Dong, S. Shape-Control of Pt-Ru Nanocrystals: Tuning Surface Structure for Enhanced Electrocatalytic Methanol Oxidation. *J. Am. Chem. Soc.* **2018**, *140* (3), 1142−1147.
(23) Beermann, V.; Gocyla, M.; Willinger, E.; Rudi, S.; Heggen, M.; Dunin-Borkowski, R. E.; Willinger, M.-G.; Strasser, P. Rh-Doped Pt-Ni Octahedral Nanoparticles: Understanding the Correlation between Elemental Distribution, Oxygen Reduction Reaction, and Shape Stability. *Nano Lett.* **2016**, *16*, 1719−1725.
(24) Stamenkovic, V.; Mun, B. S.; Mayrhofer, K. J. J.; Ross, P. N.; Markovic, N.; Rossmeisl, J.; Greeley, J.; Nørskov, J. K. Changing the Activity of Electrocatalysts for Oxygen Reduction by Tuning the Surface Electronic Structure. *Angew. Chem., Int. Ed.* **2006**, *45*, 2897−2901.
(25) Stamenkovic, V. R.; Fowler, B.; Mun, B. S.; Wang, G.; Ross, P. N.; Lucas, C. A.; Marković, N. M. Improved Oxygen Reduction Activity on $Pt_3Ni(111)$ via Increased Surface Site Availability. *Science* **2007**, *315*, 493−497.
(26) Carpenter, M. K.; Moylan, T. E.; Kukreja, R. S.; Atwan, M. H.; Tessema, M. M. Solvothermal Synthesis of Platinum Alloy Nanoparticles for Oxygen Reduction Electrocatalysis. *J. Am. Chem. Soc.* **2012**, *134* (20), 8535−8542.
(27) Cui, C.; Gan, L.; Neumann, M.; Heggen, M.; Cuenya, B. R.; Strasser, P. Carbon Monoxide-Assisted Size Confinement of Bimetallic Alloy Nanoparticles. *J. Am. Chem. Soc.* **2014**, *136*, 4813−4816.
(28) Tian, X.; Zhao, X.; Su, Y.-Q.; Wang, L.; Wang, H.; Dang, D.; Chi, B.; Liu, H.; Hensen, E. J. M.; Lou, X. W. D.; Xia, B. Y. Engineering bunched Pt-Ni alloy nanocages for efficient oxygen reduction in practical fuel cells. *Science* **2019**, *366*, 850−856.
(29) Gan, L.; Heggen, M.; O'Malley, R.; Theobald, B.; Strasser, P. Understanding and Controlling Nanoporosity Formation for Improving the Stability of Bimetallic Fuel Cell Catalysts. *Nano Lett.* **2013**, *13*, 1131−1138.
(30) Feng, Q.; Zhao, S.; He, D.; Tian, S.; Gu, L.; Wen, X.; Chen, C.; Peng, Q.; Wang, D.; Li, Y. Strain Engineering to Enhance the Electrooxidation Performance of Atomic-Layer Pt on Intermetallic Pt_3Ga. *J. Am. Chem. Soc.* **2018**, *140*, 2773−2776.
(31) Wang, C.; Chi, M.; Li, D.; Strmcnik, D.; van der Vliet, D.; Wang, G.; Komanicky, V.; Chang, K.-C.; Paulikas, A. P.; Tripkovic, D.; Pearson, J.; More, K. L.; Markovic, N. M.; Stamenkovic, V. R. Design and Synthesis of Bimetallic Electrocatalyst with Multilayered Pt-Skin Surfaces. *J. Am. Chem. Soc.* **2011**, *133*, 14396−14403.
(32) Li, J.; Li, L.; Wang, M. J.; Wang, J.; Wei, Z. Alloys with Pt-skin or Pt-rich surface for electrocatalysis. *Curr. Opin. Chem. Eng.* **2018**, *20*, 60−67.
(33) Stephens, I. E. L.; Bondarenko, A. S.; Perez-Alonso, F. J.; Calle-Vallejo, F.; Bech, L.; Johansson, T. P.; Jepsen, A. K.; Frydendal, R.; Knudsen, B. P.; Rossmeisl, J.; Chorkendorff, I. Tuning the Activity of Pt(111) for Oxygen Electroreduction by Subsurface Alloying. *J. Am. Chem. Soc.* **2011**, *133*, 5485−5491.
(34) Schaefer, Z. L.; Gross, M. L.; Hickner, M. A.; Schaak, R. E. Uniform Hollow Carbon Shells: Nanostructured Graphitic Supports for Improved Oxygen-Reduction Catalysis. *Angew. Chem., Int. Ed.* **2010**, *49*, 7045−7048.
(35) Porter, N. S.; Wu, H.; Quan, Z.; Fang, J. Shape-Control and Electrocatalytic Activity-Enhancement of Pt-Based Bimetallic Nanocrystals. *Acc. Chem. Res.* **2013**, *46* (8), 1867−1877.
(36) Gan, L.; Cui, C.; Heggen, M.; Dionigi, F.; Rudi, S.; Strasser, P. Element-specific anisotropic growth of shaped platinum alloy nanocrystals. *Science* **2014**, *346* (6216), 1502−1506.
(37) Niu, Z.; Becknell, N.; Yu, Y.; Kim, D.; Chen, C.; Kornienko, N.; Somorjai, G. A.; Yang, P. Anisotropic phase segregation and migration of Pt in nanocrystals en route to nanoframe catalysts. *Nat. Mater.* **2016**, *15*, 1188−1194.
(38) Gong, W.; Jiang, Z.; Wu, R.; Liu, Y.; Huang, L.; Hu, N.; Tsiakaras, P.; Shen, P. K. Cross-double dumbbell-like Pt−Ni nanostructures with enhanced catalytic performance toward the reactions of oxygen reduction and methanol oxidation. *Appl. Catal., B* **2019**, *246*, 277−283.
(39) Gong, W.; Jiang, Z.; Huang, L.; Shen, P. K. Pt-Ni alloy hyperbranched nanostructures with enhanced catalytic performance towards oxygen reduction reaction. *Int. J. Hydrogen Energy* **2018**, *43*, 18436−18443.

https://dx.doi.org/10.1021/acsaem.9b01930
ACS Appl. Energy Mater. 2020, 3, 768−776

(40) Jiang, Z.; Liu, Y.; Huang, L.; Gong, W. H.; Shen, P. K. A Facile Method to Synthesize Pt-Ni Octahedral Nanoparticles with Porous and Open Structure Features for Enhanced Oxygen Reduction Catalysis. *ACS Sustainable Chem. Eng.* **2019**, *7*, 8109−8116.
(41) Zhao, M.; Holder, J.; Chen, Z.; Xie, M.; Cao, Z.; Chi, M.; Xia, Y. Facile Synthesis of Pt Icosahedral Nanocrystals with Controllable Sizes for the Evaluation of Size-Dependent Activity toward Oxygen Reduction. *ChemCatChem* **2019**, *11*, 2458.
(42) Song, X.; Luo, S.; Fan, X.; Tang, M.; Zhao, X.; Chen, W.; Yang, Q.; Quan, Z. Controlled Synthesis of PtNi Hexapods for Enhanced Oxygen Reduction Reaction. *Front. Chem.* **2018**, *6* (468), 1−8.
(43) Oh, A.; Baik, H.; Choi, D. S.; Cheon, J. Y.; Kim, B.; Kim, H.; Kwon, S. J.; Joo, S. H.; Jung, Y.; Lee, K. Skeletal Octahedral Nanoframe with Cartesian Coordinates via Geometrically Precise Nanoscale Phase Segregation in a Pt@Ni Core-Shell Nanocrystal. *ACS Nano* **2015**, *9* (3), 2856−2867.
(44) Chen, S.; Wu, H.; Tao, J.; Xin, H.; Zhu, Y.; Chen, J. Pt−Ni Seed-Core-Frame Hierarchical Nanostructures and Their Conversion to Nanoframes for Enhanced Methanol Electro-Oxidation. *Catalysts* **2019**, *9* (1), 39.
(45) Kwon, H.; Kabiraz, M. K.; Park, J.; Oh, A.; Baik, H.; Choi, S.-I.; Lee, K. Dendrite-Embedded Platinum-Nickel Multiframes as Highly Active and Durable Electrocatalyst toward the Oxygen Reduction Reaction. *Nano Lett.* **2018**, *18* (5), 2930−2936.
(46) Wang, X.; Ruditskiy, A.; Xia, Y. Rational design and synthesis of noble-metal nanoframes for catalytic and photonic applications. *Nat. Sci. Rev.* **2016**, *3*, 520−533.
(47) Liu, H.-l.; Nosheen, F.; Wang, X. Noble metal alloy complex nanostructures: controllable synthesis and their electrochemical property. *Chem. Soc. Rev.* **2015**, *44* (10), 3056−3078.
(48) Luo, L.; Duan, Z.; Li, H.; Kim, J.; Henkelman, G.; Crooks, R. M. Tunability of the Adsorbate Binding on Bimetallic Alloy Nanoparticles for the Optimization of Catalytic Hydrogenation. *J. Am. Chem. Soc.* **2017**, *139*, 5538−5546.
(49) Luo, L.; Zhang, L.; Duan, Z.; Lapp, A. S.; Henkelman, G.; Crooks, R. M. Efficient CO Oxidation Using Dendrimer-Encapsulated Pt Nanoparticles Activated with < 2% Cu Surface Atoms. *ACS Nano* **2016**, *10*, 8760−8769.
(50) Zhuang, H.; Tkalych, A. J.; Carter, E. A. Understanding and Tuning the Hydrogen Evolution Reaction on Pt-Covered Tungsten Carbide Cathodes. *J. Electrochem. Soc.* **2016**, *163* (7), 629−636.
(51) Multi-Year Research, Development and Demonstration Plan: Planned Program Activities for 2011−2020; Department of Energy, 2012.
(52) Sztaberek, L.; Mabey, H.; Beatrez, W.; Lore, C.; Santulli, A. C.; Koenigsmann, C. Sol−Gel Synthesis of Ruthenium Oxide Nanowires To Enhance Methanol Oxidation in Supported Platinum Nanoparticle Catalysts. *ACS Omega* **2019**, *4* (10), 14226−14233.
(53) Chen, S.; Thota, S.; Singh, G.; Aímola, T. J.; Koenigsmann, C.; Zhao, J. Synthesis of hollow Pt−Ag nanoparticles by oxygen-assisted acid etching as electrocatalysts for the oxygen reduction reaction. *RSC Adv.* **2017**, *7* (74), 46916−46924.
(54) Koh, S.; Strasser, P. Electrocatalysis on Bimetallic Surfaces: Modifying Catalytic Reactivity for Oxygen Reduction by Voltammetric Surface Dealloying. *J. Am. Chem. Soc.* **2007**, *129* (42), 12624−12625.
(55) Wang, C.; Markovic, N. M.; Stamenkovic, V. R. Advanced Platinum Alloy Electrocatalysts for the Oxygen Reduction Reaction. *ACS Catal.* **2012**, *2*, 891−898.
(56) Garsany, Y.; Baturina, O. A.; Swider-Lyons, K. E.; Kocha, S. S. Experimental Methods for Quantifying the Activity of Platinum Electrocatalysts for the Oxygen Reduction Reaction. *Anal. Chem.* **2010**, *82* (15), 6321−6328.
(57) Zhang, L.; Iyyamperumal, R.; Yancey, D. F.; Crooks, R. M.; Henkelman, G. Design of Pt-Shell Nanoparticles with Alloy Cores for the Oxygen Reduction Reaction. *ACS Nano* **2013**, *7* (10), 9168−9172.
(58) Zhang, L.; Henkelman, G. Computational Design of Alloy-Core@Shell Metal Nanoparticle Catalysts. *ACS Catal.* **2015**, *5*, 655−660.
(59) Markovic, N.; Gasteiger, H.; Ross, P. N. Kinetics of Oxygen Reduction on Pt(hkl) Electrodes: Implications for the Crystallite Size Effect with Supported Pt Electrocatalysts. *J. Electrochem. Soc.* **1997**, *144* (5), 1591−1597.

https://dx.doi.org/10.1021/acsaem.9b01930
ACS Appl. Energy Mater. 2020, 3, 768−776